Wind tunnel investigation on a squared–back commercial vehicle

AIMETA 2017
XXIII Conference
The Italian Association of Theoretical and Applied Mechanics
Luigi Ascione, Valentino Berardi, Luciano Feo, Fernando Fraternali and Antonio Michele Tralli (eds.)
Salerno, Italy, 4–7 September 2017

WIND TUNNEL INVESTIGATION ON A SQUARED-BACK COMMERCIAL VEHICLE

Costantino Sardu[1], Juan J. Cerutti[1] and Gaetano Iuso[1]

[1]Politecnico di Torino
Corso Duca degli Abruzzi 24, Torino.
e-mail: costantino.sardu@polito.it, juan.cerutti@polito.it, gaetano.iuso@polito.it

Keywords: Car aerodynamics, drag measurement

Abstract. *The assessment of an appropriate methodology for a wind tunnel investigation on a square back vehicle model is presented and discussed. The $C_D - Re$ curve is evaluated in order to identify the adequate range of Reynolds number for the tests. The drag coefficient value is attested at $C_D = 0.465$ which is in accordance with the literature results for the same category of vehicles considered. The repeatability and the accuracy of the C_D have been analyzed through a campaign of measurements and an error propagation analysis is dedicated to associate the correct uncertainty to the drag coefficient values. The analysis of statistical convergence of the measured quantities is also carried out in order to fix the adequate acquisition time. The results of the experimental investigation regarding the measurement methodology, drag coefficient, base pressure distribution, position of the center of pressure, and wake measurements are presented highlighting the main natural flow features. Moreover, the pressure fluctuations measured by microphone sensors allowed to evidence the unsteadiness and possible flow configurations involving the entire rear part.*

1 INTRODUCTION

In the last years the CO_2 emission has become one of the major environment issue, and several nations are implementing more restrictive regulations to decrease the generation of this atmosphere-harmful compose. In case of commercial vehicles, the nature of their utilization has the priority and requires the optimization of the internal volume and the functionality. Consequently, the external shape presents the squared back configuration to which is inevitably associated a high aerodynamic drag because of the presence of a wide separated flow region and therefore considerable pressure losses.

Several passive devices (as wings, vertical splitter plate, vortex generators, etc.[1]) have been tested through the years reaching interesting results on the aerodynamic performances. For the same reason, the flow control based on jets, continuous, unsteady or synthetic are drawing the attention of car aerodynamics researchers in the recent years due to their relatively simple application. Different studies, in fact, have been performed on these techniques, some of the more relevant are the ones of Rouméas et al. [2] and Littlewood et al. [3]. Rouméas and Gilliéron [2] settled a group of 4 jets disposed on the periphery of square back semi-infinite body. This last CFD study examined the effect of the injection angle and intensity of the outcoming flow from the jet slot, obtaining a maximum aerodynamic drag reduction up to 29%. Littlewood and Passmore[3] tested in a wind tunnel facility a modified Windsor body, which presents a more realistic sloped front with respect to the classic Ahmed body, and a truncated rear part. They investigated the effect of using a continuous jet on the upper edge of the rear part. The jet could be settled at 4 different angles with a variable intensity. The authors found in this experimental work, that a drag reduction up to 12% can be reached with their technique. Recently, further flow control studies based on unconventional jets were proposed in order to reduce the drag of square back vehicles. A group of arrays of microjets were investigated by McNally et al.[4], this technique, applied to a the base periphery of a square back model presented a low level of drag reduction, i.e. 3% but with a favorable energy budget. Schmidt et al.[5] combined the forcing of the flow by means of fluidic oscillators and the boat tailing in order to reduce the drag of the squared back model. The results also in this case were encouraging leading to a drag reduction up to 20%. Despite this, main part of drag reduction can be attributed to the boat tailing which effectiveness is well known in literature [1]. Finally, Barros et al.[6] introduced a pulsed jets actuation to control the drag of a square back model. They studied the effect of the forcing frequency finding a strong dependency of the drag from this parameter. A forcing with a broadband near the natural wake time scale caused an increase of the drag and improved the wake entertainment. Conversely, high frequency forcing appeared beneficial reducing both the entertainment and consequently the drag of the body.

The present investigation considers a simplified three-dimensional model representative of transportation commercial vehicles. To this model is applied an active flow control technique based on continuous jets disposed in the periphery of the model base. A preliminary CFD investigation [7, 8] evidenced the effectiveness of the control technique and allowed to evaluate the drag sensitivity to the different flow control parameters. In the present paper, the focus is on the methodology of the tests and on the natural flow features. The work here described represents a preliminary step necessary to characterize the experiment peculiarity. The methodology to measure accurately is presented, and the error propagation analysis on the drag coefficient leads to reach high level of accuracy. Moreover, an investigation was performed to define the appropriate acquisition time for each magnitude, in a reliable way. The pressure distribution presented the wide suction region on the base surface and is also used to accurately evaluate the

drag value. Furthermore the pressure fluctuation and total pressure measurement in the wake flow highlights the flow characteristics. Finally, a comparison of different power spectra signals is used to recognize the nature of the different fluctuations measured.

2 METHODOLOGY

2.1 Model and wind tunnel

The model used in the wind tunnel investigation is presented in figure 1 with its reference axes. It is a 3D printed commercial vehicle model at a scale of 1:10. This category of vehicle presents a square back rear part as shown in the figure. The length of the model (L) is equal to $412\ mm$, measured from the front tip until the rear plane, while the width (W) is $171\ mm$. The model height (H) is $200\ mm$, and the ground clearance is $20\ mm$. Regarding to the wheels, they have a diameter of $56\ mm$ and a width of $22\ mm$. The front part presents a realistic slant angle of $50°$ and a rounded nose with a radius of $R = 46\ mm$. Around the model are distributed

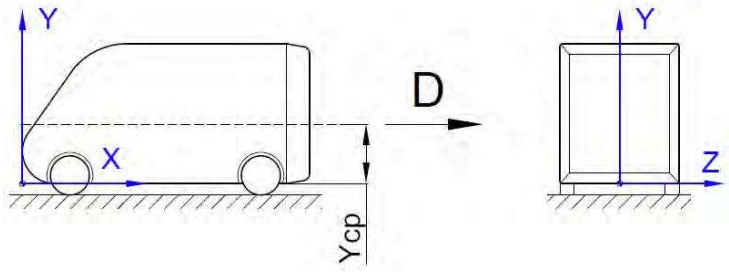

Figure 1: Axis system and position of the pressure coefficient *Ycp*.

62 pressure taps, and in particular 31 taps are disposed on the back surface, while the others cover the upper, lower and right surfaces. Settled on the rear area there is also a distribution of 16 microphones used to investigate the pressure fluctuations. Twelve of them are mounted only on the right side of the rear surface, while one microphone per surface is disposed close to the edge of the rear part, on the upper, lower and lateral surfaces. On the rear edges of the model are fitted four rectangular blowing slots which represent the flow control actuators. They have the capability of blowing air at different intensities and angles. This system is fed with compressed air, and regulated with three flow meters that controls the flow rate on the lateral, upper and lower slots.

The wind tunnel used is an open circuit facility. It has a rectangular test chamber section of $1100\ mm$ x $900\ mm$ and a total chamber length of $6000\ mm$, and is characterized by a contraction ratio of 10 connecting the settling chamber and the test chamber. Two electric motors drive two axial propellers, that allows to set a maximum free stream velocity of 12 m/s. Moreover, on the exit of the convergent part, a turbulence grid is mounted. This grid produces an homogeneous turbulent flow with a turbulence intensity equal to 7% measured at the model position (1900 mm from the grid). The grid is made with 20 mm square rods, separated uniformly by 65 mm between centers, and its function is to promote a fully turbulent flow separation on the model according to [9, 10]. To reduce the growing of the boundary layer on the lower wall of the test chamber, a suction slot of $250\ x\ 5\ mm$ is settled after the grid, transversal to the streamwise direction. This slot is connected to a vacuum pump that can be regulated varying the flow rate, achieving a maximum aspiration of $70.4\ Lts/s$.

2.2 Measurement techniques and data reduction

The model is linked to a load cell on the top of the test chamber through a sting, as shown in figure 2. A leverage system multiplies the force applied to the model and transmits it to the load cell, and the value of the drag force is obtained as shown by Sardu et al.[7].

The load cell has a full scale of $\pm 2\ Kg_f$ and an accuracy of $\pm 0.002\%$ FS. The signal of the load sampled at 1000 Hz and a sampling time of 240s.

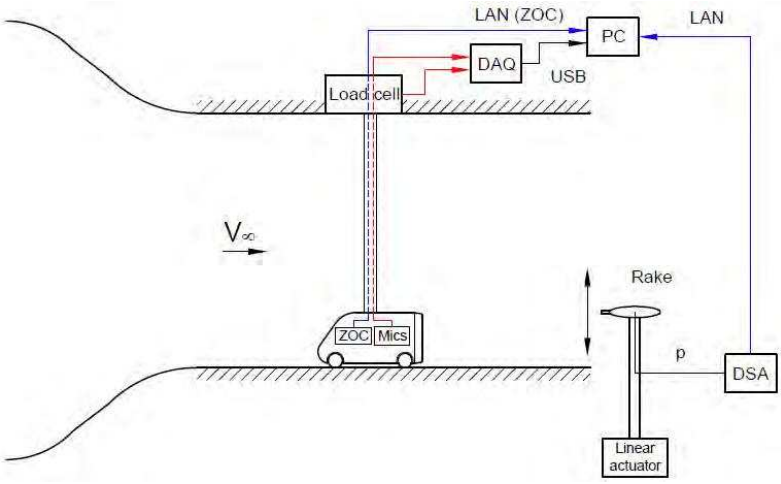

Figure 2: Simplified measurement diagram.

The pressure values on the model surfaces are measured by a ZOC33 pressure transducer from Scanivalve, with 64 input channels. This device has a full scale of $\pm 2.5kPa$, an accuracy of = $\pm 0.15\%$ FS, and a maximum sampling frequency of 500 Hz. This transducer is settled inside of the model in order to reduce the length of the pneumatic lines to their minimum. In the tests performed, the acquisition parameters for the ZOC33 were a sampling frequency of 40 Hz and sampling time of 240 s. The pressure measurements are expressed in terms of mean pressure coefficient, defined in relation 1. The fluctuations associated to these same signals from the pressure taps are represented by the pressure coefficient rms, defined in relation 2.

$$c_{p_i} = \frac{\overline{p_i(j)} - \overline{p_\infty}}{q_\infty} \tag{1}$$

$$c_{p_{RMS_i}} = \frac{p_{RMS_i}}{q_\infty} = \frac{\sqrt{\frac{1}{N-1}\Sigma_{j=1}^{N}(p_i(t_j) - \overline{p_i})^2}}{q_\infty} \tag{2}$$

where $p_i(t_j)$ is the instantaneous pressure signal of the i_{th} pressure tap at the discrete time t_j. The free stream static pressure p_∞ coincides with the atmospheric pressure and q_∞ is the freestream dynamic pressure on the test section.

The pressure fluctuations on the rear of the model are captured by the microphones distribution. This microphones are electret capacitive sensors, with a flat response in the range of 50-13000 Hz and a sensitivity of (-60 ± 3) dB. The pressure fluctuations are analyzed in terms of cross correlation function $R(i, j)$, defined as:

$$R(i,j) = \frac{\overline{p_i'(t) \cdot p_j'(t)}}{\sqrt{\overline{p_i'(t)^2}} \cdot \sqrt{\overline{p_j'(t)^2}}} \tag{3}$$

where $p_i'(t)$ are the pressure fluctuations. The indexes $i,\ j$ are the microphone identification. The values $1\ to\ 4$ refers to the microphones placed on the rear edges of the lateral surfaces, and $5\ to\ 16$ to the microphones of the rear base. For the microphones, the acquisition parameters are a sampling frequency of 10 kHz and a sampling time of 15 s.

The wake of the model is investigated using a rake, which is composed by 64 total pressure probes distributed over an horizontal support having a total width of 720 mm. The probe spacing ranges from the 7.5 mm in the central part up to 105 mm from the centerline, then the spacing becomes 15 mm up to 300 mm from the centerline, and finally the spacing of 20 mm covers the external part. The rake is positioned downstream the model at a distance s=600 mm from the model rear base, corresponding to $s/L = 1.46$. A linear actuator allows its movement on the vertical axis with steps of 30 mm from the bottom, as shown in figure 2.

To measure the pressure signals from the probes of the rake two Scanivalve DSA 3217 pressure transducers are used. Each device has 16 temperature compensated piezoresistive pressure sensors. This device has a full scale of $\pm 2400\ Pa$, an accuracy of $\pm 0.4\%$ FS and features a 16 bit of resolution A/D converter. Moreover, it has an auto zero offset correction and maximum sampling rate of 20 Hz. The wake data were collected at a sampling frequency of 20 Hz and a sampling time of 270 s.

The measurements results are represented in terms of total pressure coefficient, defined as:

$$c_{p^o}(y,z) = \frac{\overline{p^o(y,z) - p_\infty}}{q_\infty} \tag{4}$$

The data acquisition of signals from the microphones and load cell was provided by a National Instruments CDAQ chassis. Six National Instruments *9215* analog to digital acquisition modules were mounted, with 4 analog inputs each. This setup is capable of simultaneously reading 24 analog differential channels at a maximum sampling rate of $100\ kHz$ with an A/D resolution of 16 bit, and a voltage FS of $\pm 10V$.

On figure 2 is displayed a simplified diagram of the measurement chain of the tests. The signal generated by the microphones and the load cell are transmitted to the data acquisition board (DAQ) and the data are sent to the PC via USB. The data from the ZOC33 and DSA 3217 are directly sent to the PC via LAN connection. During the tests the data from the ZOC33, load cell and microphones are sampled simultaneously and with the same starting time. Conversely, the data from the DSA 3217 (wake measurements) were obtained on separated tests. All the data acquired by the ZOC33, DSA 3217 and CDAQ were managed by a Labview in-house program.

3 RESULTS

Relevant observations regarding the $C_D - Reynold$'s behavior, main flow features and accuracy of the measurements are presented. The dynamic response of the pressure fluctuations and of the load cell are described and commented.

3.1 Drag characterization and accuracy

A campaign of preliminary tests was performed in order to evaluated the dependency of the drag coefficient with respect to the Reynolds number. The maximum speed of the wind

tunnel allows to test the model at a Reynolds number of $Re_L =\simeq 2.5 \cdot 10^5$ which is lower than the real Reynolds number of a car ($Re_{Real} =\simeq 10^7$). For this reason a turbulence grid was placed in the inlet of the test section, in order to generate a level of turbulence sufficient to promote transition and virtually test at higher Reynolds number as demonstrated by Taylor in [9, 10]. The turbulence grid used was previously dimensioned and calibrated in order to promote the flow transition at post-critical flow regime of a circular cylinder with a diameter equal to $D = 200\ mm$ developed by Orazi[11]. The Reynolds dependency of the model C_D is

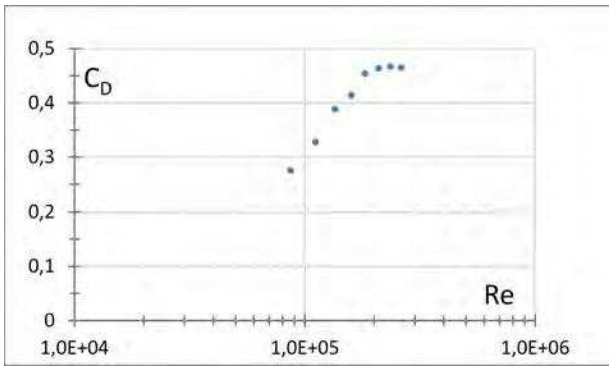

Figure 3: C_D versus Reynolds number of the car model

illustrated in Fig.3. The rising of the Reynolds number causes a growth of the drag coefficient up to a flat region. When the Reynolds number is higher than $Re_L \simeq 1.8 \cdot 10^5$, the drag coefficient appears nearly constant with a value of 0.465, which is in good accordance with the values present in literature for the same category of vehicles.

This C_D growth on the first range of Reynolds can be associated with the post-critical behavior of bluff bodies. This growth in fact is typical also of the flow around reference bluff body as 2-D cylinder and sphere. In figure 4 from the studies of Rodriguez et at. [12], different data on $C_D - Re$ of a 2D cylinder are illustrated.

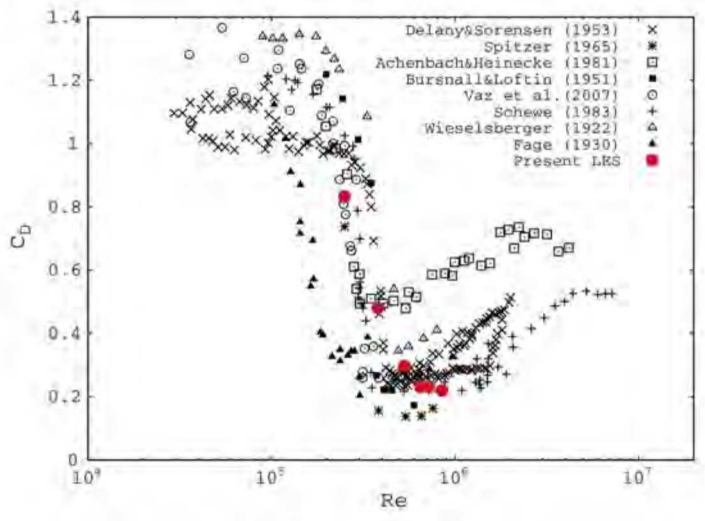

Figure 4: C_D versus Reynolds number of 2-D circular cylinder [12]

As can be seen in figure 4, after the critical Reynolds number, the C_D drops reaching the lowest value $C_{D_{min}}$. Then a rise of the drag coefficient is attested up to the Reynold number

of $Re \simeq 0.5 \cdot 10^7$. This increase of the values of the C_D reaches nearly the double of the minimum $C_{D_{min}}$. After the rising, a stabilization of the drag coefficient is measured for the cylinder. Considering the results of figure 3, many characteristics in common with the curve of the 2-D cylinder of figure 4 are observed, giving confidence on the values obtained in the present investigation.

A campaign of measurements was performed in order to evaluate the repeatability and the presence of hysteresis problems due to the leverage systems. This study consisted in repeating several identical natural flow tests.The error associated to the repeatability of the test was defined as:

$$Err_{RH}[\%] = \frac{D_{ref} - D_n}{D_{ref}} \cdot 100 \tag{5}$$

where the subscripts ref and n indicate the reference test and the number of the test considered. From this investigation was highlighted a maximum deviation Err_{RH} around 0.75%, highlighting the reliability of the experimental apparatus for the drag measurements and also with respect to the procedure assessed for the test execution.

A second investigation aimed to associate a level of accuracy of the computed drag coefficient C_D was also performed. In this case, due to the dependency of the C_D on a consistent number of measured and post-processed quantities, the error propagation analysis was performed to identify the δ_{C_D}. Following Moffat [13, 14] the subsequent relation for the uncertainty was used:

$$\delta_{C_D} = \sqrt{\sum_{i=1}^{N_p} \left(\frac{\partial C_D}{\partial x_i} \cdot \delta_{x_i} \right)^2} \tag{6}$$

The equation 6 highlights the dependency of δ_{C_D} from the product of the uncertainty δ_{x_i} and his partial derivatives $\frac{\partial C_D}{\partial x_i}$, of each parameter of the measurement x_i The final value of δ_{C_D} obtained at $Re = 2.5 \cdot 10^{-5}$ was of $\delta_{C_D} = \pm 5.67 \cdot 10^{-3}$. This δ_{C_D} corresponds to percentage error, defined as $Err_{C_D} = \frac{\delta_{C_D}}{C_D} \cdot 100\%$, equal to $Err_{C_D} = \pm 1.22\%$. The derivatives $\frac{\partial C_D}{\partial x_i}$ evidenced which parameters of the chain of measurement are crucial in order to obtain a low value of δ_{C_D} and consequently, the required attention was paid in the evaluation of these crucial parameters. The most critical parameters found are respectively the point of drag application Y_{cp} (show on figure 1), the voltage signal of the load cell and the pressure signal used to measured the free stream dynamic pressure. Thanks to this analysis, the low value of δ_{C_D} was obtained. The results on pressure distribution on the model surface and the computation of Y_{cp} are presented in the next section.

In order to obtain the values of $\overline{E}_{LC}$ and $\overline{q}_\infty$, which are namely the averaged value of the load cell and of the dynamic pressure signals, a statical approach to their measurements was adopted. This study was aimed to obtain a high level of confidence on the mean quantities and at the same time reduce the wideness of the confidence interval by measuring a higher number of samples.
Considering for example the load cell signal, the interval of confidence can be written as [15]:

$$Prob\left[\overline{E}_{LC} - \frac{\sigma_{E_{LC}} z_{\frac{\alpha}{2}}}{\sqrt{N_E}} < \mu_{E_{LC}} < \overline{E}_{LC} - \frac{\sigma_{E_{LC}} z_{\frac{\alpha}{2}}}{\sqrt{N_E}} \right] = 1 - \alpha \tag{7}$$

where $\mu_{E_{LC}}$ is the true value of the mean of the load cell signal, $\overline{E}_{LC}$ represents the mean value of the signal samples, $\sigma_{E_{LC}}$ is the standard deviation of the signal, $z_{\alpha/2}$ represents the coordinate of the standardized normal density function and finally N_E is the number of samples used to

evaluate $\overline{E}_{LC}$. Once decided the level of confidence $(1-\alpha)$, the equation 7 evidences that a growth of the number of samples N_E causes the convergence of $\sigma_{E_{LC}}$ and a contraction of the confidence interval. This property was used to set the correct sampling time that ensured a sufficiently narrow confidence interval of the parameters $\overline{E}_{LC}$ and $\overline{q}_\infty$. This lead to associate a low uncertainty to their values and consequently reducing their effect on the accurancy of the drag coefficient, according to equation 6. This statistical convergence study fixed the acquisition time to 240 s for the load cell and pressure signals, ensuring an accuracy of the averaged values of $Err_{E_{LC}} = Err_{q_\infty} = 0.05\%$ with a confidence level greater than 95%.

3.2 Pressure distribution

Figure 5 presents the pressure coefficient distributions on the base surface in three different vertical planes parallel to the free-stream velocity V_∞. The reference system used is illustrated in figure 1.

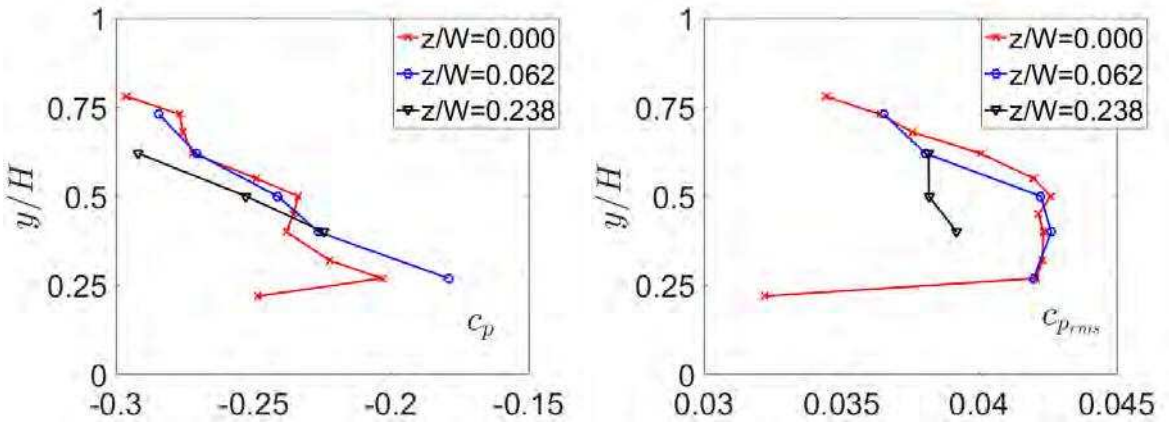

(a) c_p (b) $c_{p_{rms}}$

Figure 5: Pressure coefficients on the base surface

Figure 5a represents the behavior of the mean c_p distribution, showing a suction region present in all the base surface ranging $-0.3 < c_p < -0.17$. The intensity of this suction is higher in the upper part of the surface and a slight recovery is present in the lower part, reaching the maximum level at $y/H = 0.25$. For this kind of vehicles, which are characterized by a square back rear part, the near wake flow presents a toroidal vortex structure [16, 2]. This ring shaped vortex adheres to the base surface causing a annular distribution of the suction region and a slight recovery of pressure nearly in the center of the surface, due to the impingement of the flow. The values of figure 5a are in good accordance with the literature results, presenting a suction region in the upper part of the surface and the impingement region in the lower part. Consequently, it can be speculated that the toroidal vortex is present, however it exhibits an asymmetry with respect to the half height of the model. Figure 5b illustrates the intensity of fluctuations on the base surface. This intensity is presented in terms of $c_{p_{rms}}$ according to relation 2. The graph shows that the major level of fluctuations is reached in a interval $0.25 < y/H < 0.5$ corresponding nearly to the region of maximum c_p measured. This evidences the unsteady nature of the flow, and, in particular, the level of fluctuations rises in correspondence of the impingement region. This point, in fact, oscillates on the surface and this movement probably are responsible of the rising of pressure fluctuations. In conclusion, both

pressure coefficient distributions presented in figure5, following to the literature description, are in good accordance with a presence in the near wake region of a three-dimensional structure consisting on average in a ring shaped vortex.

The evaluation of the drag force requires the knowledge of the position of the pressure center on the y axis. To this end, the pressure distribution over the model is needed, so the pressure center is calculated.

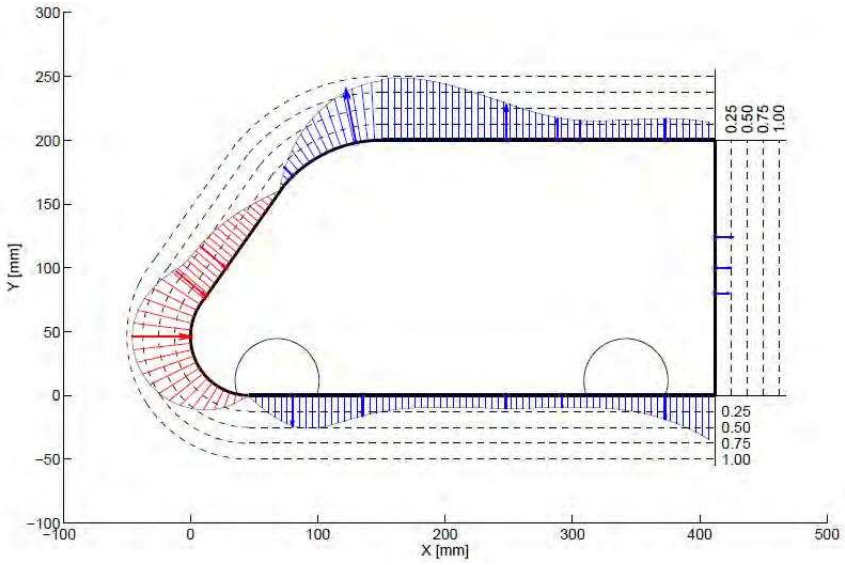

Figure 6: Pressure distribution over the model. (Re=$2,5 * 10^5$)

The pressure coefficient distribution on the surfaces of the model profile for the natural flow is shown in figure 6 . The values of the c_p are displayed with arrows whose length is proportional to the strength of the c_p module. In particular, the red arrows are for positive values while the blue color is for negative c_p values. The c_p distribution is obtained through interpolations from the measurements, and the positions of the pressure taps are indicated with circles.

In the pressure tap on the nose of the model the $c_p \approx 1$. This c_p should be equal to 1, since this pressure tap coincides with the stagnation point of the model. This slight difference can be associated with a small decrease of the free stream velocity due the effects of the boundary layer of the wind tunnel. In the top part, the c_p coefficient descend until negative values, reaching $c_p \cong -1$ at $150mm$ from the nose, and then stabilizes at -0.26 on the last part of the model. This minimum value of the c_p could be associated with the presence of the sting and consequently the acceleration of the local flow velocity. Moreover, on the lower part, two zones of high negative values of c_p (around -0.5) are observed on the near-wheel region, because the flow has a reduced passage area. On the rest of the rear surface, the value of the c_p is constant at -0.2.

The vertical position of the center of pressure (Y_{cp}) where the aerodynamic drag is applied, is obtained as:

$$Y_{cp} = \frac{1}{(\sum c_{pi} \cdot \triangle s_i \cdot cos(\theta_i))} (\sum c_{pi} \cdot \triangle s_i \cdot cos(\theta_i) \cdot y_i) \tag{8}$$

Where c_{pi} is the pressure coefficient of each pressure tap, $\triangle s_i$ is the reference length of each pressure tap, y_i is the position of the pressure tap on the vertical axis and θ_i is the angle between the x axis and the normal to the surface vector on the i_{th} pressure tap. In figure 1 the reference

coordinates and the Y_{cp} measurement are shown. Typical values of Y_{cp}, found on the test campaigns natural flow, are around $Y_{cp} = 61$ millimeters, which correspond to an non-dimensional height of $Y_{cp}/H = 0.3$, for a test Reynolds number of $2.5 \cdot 10^5$.

3.3 Cross correlation of the microphones

Figure 7 shows the results of the cross correlation function $R(i, j)$ found for the test Reynolds number of $Re_L = 2.5 \cdot 10^5$. In each map the relative reference microphone used for the computation of the cross-correlation is indicated, namely *mic 1* on the left, *mic 2* on the upper, *mic 3* on the right and *mic 4* on the bottom surfaces.

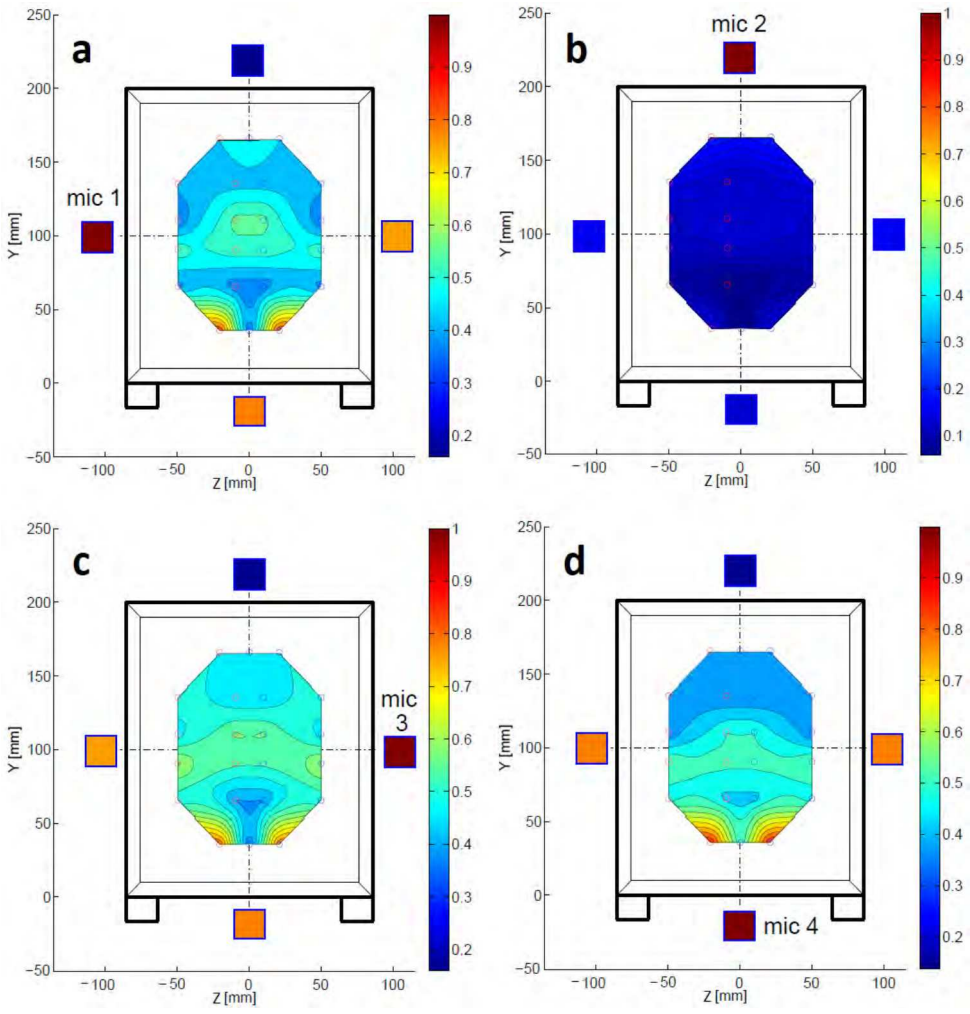

Figure 7: Cross correlation of the pressure fluctuations. (Re=$2,5 * 10^5$)

In figure 7a ($R(1, j)$), the colormap shows a high correlation of 0.8 between the signal of microphone 1 and microphones 3 and 4, and an almost null correlation with microphone 2. These cross correlation values are represented by square colored markers on the lateral surfaces of the rear profile. In regard to the microphones on the rear base surface, the correlation covers values from 0.4 to 0.5, except for the microphone settled on the lower-right position (mic 15). In this case, the correlation reaches a value of $R(1, 15) = 0.85$.

An equivalent situation happens with the $R(3, j)$, whose colormap is represented in figure

7c. In fact, equal values of R were obtain regarding microphones 1,2 and 4, but with a range of correlation slightly higher, between 0.5 and 0.6 on the rear base. These colormap behavior can be associated with the fact that the microphones are placed on the right side of the surface, hence are closer to the microphone 3 than the microphone 1. Moreover, the same behavior of the lower-right microphone (mic 15) is observed, with a value of the cross-correlation $R(3, 15) = 0.85$. In fig. 7.d is shown the colormap for *mic 4*. The cross correlation with microphones 1 and 3 is 0.8 and almost null with microphone 2, as in the cases *a* and *c*. Regarding to the rear base, it presents a high correlation with the lower-right microphone (mic 15) as in cases *a* and *c*, of about 0.85. On the rest of the surface the correlation variates from 0.4 to 0.55, with the lowest correlations with the microphone placed on the upper part of the rear surface. Finally, considering *mic 2* as a reference, the values of the cross-correlation $R(2, j)$ are shown in figure 7b. In this case, the value of the correlation is below 0.15 for all the microphones.

As seen in figure 7 *a*,*c* and *d*, a high correlation is found for right, left and bottom microphones, because they are sensing the same incoming flow around the model. As anticipated in section 3.2, for this kind of geometry, the features of the wake can be asociated to a toroidal vortex structure highly unsteady, as also demonstrated by Rouméas et al. [2]. The result reported in the colormaps are highly related with the wake configuration. In fact, this large scale flow structure involve the whole rear base of the model, hence the four microphones on the lateral faces are influenced from the same vortex structure originated in the rear edges. Particularly high is the cross correlation with the mic 15, for all the lateral microphones. This behavior could be associated with an asymmetrical vortex structure behind the model, in the vertical direction. This may be the cause of the high correlations measured with the lower part of the model and the lateral microphones.

The presence of the sting in the upper part of the model (as seen in figure 2) produces horseshoe vortex close to the top surface, and this aerodynamic structure produces oscillations on the flow largely different than the surrounding flow field. This may be the reason of the almost null cross correlations refereed to the mic 2.

3.4 Wake analysis

The wake measurements performed with the rake of total pressure probes represent an important diagnostic technique which evidences the region of losses caused by the presence of the body. The wake flow, in fact, contains all the information of the flow losses, and the drag value can be also computed through the integration of the velocity and pressure distribution on the wake. The present wake investigation is not aimed to evaluate the drag which is directly measured by the load cell, however it is used to evidence the different region of losses and, subsequently it will be useful to evidence the flow control effect.

In figure 8 are shown the total pressure coefficient distributions in the wake according to the reference system presented in figure 1. In particular, figure 8a shows several distributions on vertical planes parallel to the symmetry plane of the rear of the model, whereas the Figure 8b presents the c_{p° distributions on the planes parallel to the wind tunnel wall. The wake flow exhibits a total extension of $y/H \simeq 1.5$ in the vertical direction, while in the spanwise direction the wake is extended up to $z/W \simeq 1.2$. Note that the origin of z axis is set on the symmetry plane of the model. On figure 8 can be observed that a region of main losses is reached in a range of $0.3 < y/H < 0.8$ on the lateral view, and $0.3 < z/W < 0.6$ on the top view, where the total pressure coefficient reaches a minimum value of $c_{p^\circ} \simeq 0.6$. Considering a constant ratio y/H and with the increasing of the value of z/W, the total pressure coefficient tends to become the value of the freestream flow. In the top view (figure 8b) the results evidence the

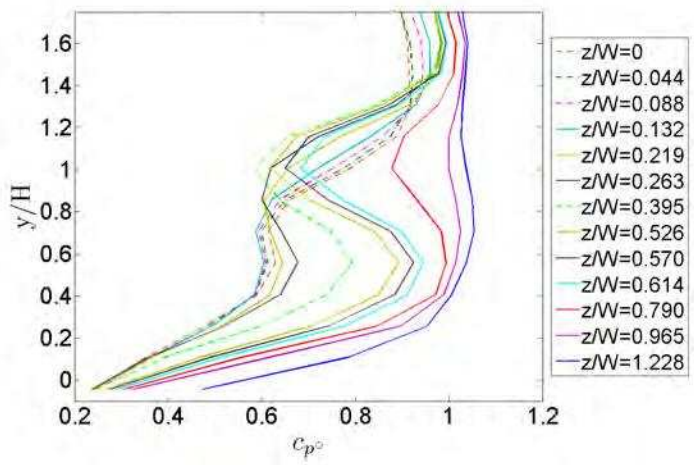

(a) Lateral view

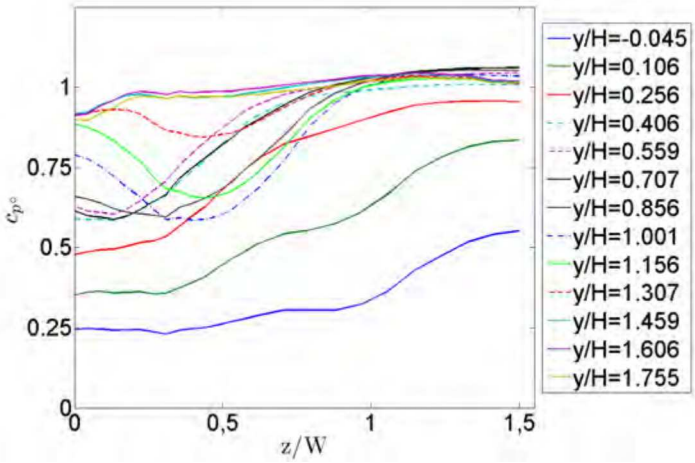

(b) Top view

Figure 8: Total pressure distribution in the wake flow, distance $x/L = 1.46$

losses related to the boundary layer. The particular behavior of the total pressure coefficient distribution on both vertical and horizontal planes can be associated to the vortex structures downstream the model. In the upper part of the wake, the data exhibit the presence of the corner vortex, originated by the flow interaction between the lateral surface and the top surface. This flow structure cause the main losses at $z/W = 0.5$ which is the position of the lateral surface of the model. The effect of this vortex structure is perceived up to $y/H \simeq 1.4$ and $z/W \simeq 1.4$.

3.5 Spectrum analysis results

In figure 9 are displayed the power spectra of a microphone and a pressure tap signals on the near center of the rear base ($y/H \approx 0.5$, $z/W \approx 0.5$), and load cell signals. Two different power spectra of the load cell signal are shown, one related to the natural flow and the other to the free oscillation case. This last spectrum is obtained through an impact test, consisting on giving an impulse in the direction of the free stream velocity (i.e. the drag direction), to the model's front part.

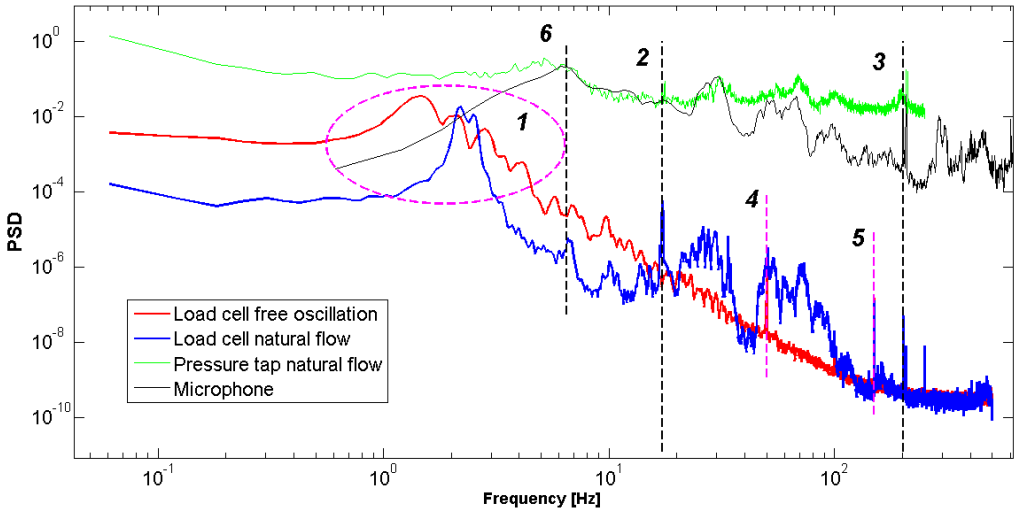

Figure 9: Power spectra of the signals of a microphone and a pressure tap a the load cell during a natural flow test and power spectra of the load cell in free oscillation condition

The first observation from the graph is the different magnitudes between the pressure tap and microphone, and the load cell power spectra. This is due to the signal nature: the load cell provides an electrical signal, then the power spectrum is expressed in $[Volt^2 \cdot s]$, while the pressure tap and microphones give a pressure signal, meaning that the power spectra are expressed in $[Pa^2 \cdot s]$.

In regard to the spectrum of the load cell on free oscillations, there is a first area on the low frequency region indicated by the number 1 in which is present a peak power density centered in a frequency of 1.5 Hz. In the natural flow case, the maximum power density is present at a slightly higher frequency of 2.2 Hz. The shift on this last frequency could be legated to the different conditions in which the measurements were taken, due to the the different equilibrium positions of the drag measurement system. This high power density zone is not present on the signals of the microphone and pressure tap, meaning that are due to mechanical oscillations at natural frequencies of the drag measurement system on both free oscillation and natural flow cases. On Fig. 9 with the numbers 2 and 3 are shown two peaks at 17 Hz and 202 Hz of the power spectra present on the microphone, pressure tap and the load cell of the natural flow. These peaks coincide with the fluctuations introduced by the fans of the wind tunnel, and they are evaluated considering the RPMs and the number of blades, as $f_{1blade} = \frac{1000RPM}{60} = 16.67\ Hz$ and $f_{12blade} = 12 \cdot \frac{1000RPM}{60} = 200\ Hz$. These forcing frequencies are generated by the passing by of the blades of the fans. The peaks indicated with 4 and 5 in figure 9 respectively at 50 HZ and 150 Hz, are disturbs due to the power supply frequency of the entire system,

and consequently are present also in the free oscillation spectrum of the load cell signal. The pressure tap does not capture this effect due to the different instrumentation used.

Finally, a peak of energy is present on the microphones and pressure taps shown on the reference 6 of figure 9, at a frequency equal to 6.5 Hz. The associated Strouhal number is:

$$St = \frac{f \cdot H}{V_\infty} \tag{9}$$

The value of the Strouhal of the test at $V_\infty = 9\ m/s$, the peak frequency at $6,5Hz$ and the height of the model $H = 0.2$ is equal to $St = 0.144$. This value corresponds with the typical values of vortex shedding for bluff bodies (≈ 0.2) and for square back Ahmed body found by Volpe et al. [17] (≈ 0.13). Around the frequencies of 30 Hz and 70 Hz are present two zones of high power density concentration, observed on the signals of microphone, pressure tap and load cell. Those power concentrations may be associated with the effect of the turbulence grid. Since the grid's characteristic dimensions are 0.065 m for the distance between grid elements and 0.02 m for the grid element width, the Strouhal number values are 0.155 and 0.21 respectively. Consequently, the region of power concentration may be explained with the vortex shedding released by the grid bars.

4 CONCLUSIONS

The analysis of the wind tunnel methodology on a square back vehicle model is illustrated. The natural flow is used as reference case for the subsequent investigation on flow control effectiveness and the methodology is assessed on this reference case. The $C_D - Re$ curve is illustrated and, from the assessment of the methodology, a Reynolds number equal to $Re_L \simeq 2.5 \cdot 10^5$ was considered because for $Re_L > 1.8 \cdot 10^5$ the drag coefficient exhibits no sensitivity to this fluid dynamic parameter. Moreover, $Re_L \simeq 2.5 \cdot 10^5$ guarantees a measurement of C_D equal to the literature values.

The reliability of the methodology is also discussed in terms of accuracy of the drag measurement, and the chain of measurements ensures a repeatability and hysteresis error of $Err_{RH} = 0.75\%$. The error propagation analysis individuates the most critical parameters and determines the accuracy of the drag coefficient, ascribing a percentage error of $Err_{C_D} = \pm 1.22\%$. To reach this low level of error, the statistical convergence of the main measured quantities is also performed and this study leads to set the total sampling time equal to 240 s.

The pressure distribution on the model assumes fundamental importance because is used not only as a diagnostic technique of the flow features, but also in the calculation of the center of pressure, which for the tests performed was $Y_{cp} \approx 61mm$. Both the pressure distribution on the base surface and the wake measurement allows to understand the main features of the separated flow, and the losses that cause the drag force. As expected, in correspondence of model base, a consistent total pressure deficit is measured. Finally, the corner vortex originated by the flow from the lateral and upper surfaces is noticed in the total pressure measurements and appeared a not negligible contribution to the total losses of the flow.

The spectra analysis of the measured signals from the Load cell, microphones and pneumatic line, is performed. The mechanical free oscillation response of the drag measurement mechanism is measured and characterized. Moreover, the effects of the blade rotation and turbulence grid are also identified as spurious contributions. Finally, a high power zone is found at 6.5 Hz, corresponding to a Strouhal number of $St = 0.14$ typical of the vortex shedding for this kind of body.

REFERENCES

[1] H. Choi, J. Lee, and H. Park, *Aerodynamics of heavy vehicles*. Annual Review of Fluid Mechanics, 46, 441-468, 2014.

[2] M. Rouméas, P. Gilliéron, and A. Kourta, *Analysis and control of the near-wake flow over a square-back geometry*. Computers and Fluids, 38(1):6070, 2009.

[3] R.P. Littlewood and M.A. Passmore, *Aerodynamic drag reduction of a simplified square-back vehicle using steady blowing*. Exp Fluids 53:519529, 2012.

[4] J. McNally, E.Fernandez, G. Robertson, R. Kumar, K.Taira, F. Alvi, Y. Yamaguchi and K. Murayama, *Drag reduction on a flat-back ground vehicle with active flow control*. Journal of Wind Engineering and Industrial Aerodynamics, 145, 292-303, 2015.

[5] H. J. Schmidt, R. Woszidlo, C. N. Nayeri and C. O. Paschereit, *Drag reduction on a rectangular bluff body with base flaps and fluidic oscillators*. Experiments in Fluids, 7(56), 1-16, 2015.

[6] D. Barros, J. Bore, B. R. Noack, A. Spohn and T.Ruiz, *Bluff body drag manipulation using pulsed jets and Coanda effect*. Journal of Fluid Mechanics, 805, 422-459, 2016.

[7] C. Sardu, S. Sedda, and G. Iuso., *Flow separation control applied to simplified car*. Proceedings of AIDAA XXIII, Torino 17-19 Nov 2015.

[8] C. Sardu, S. Sedda, and G. Iuso, *Wake control of a 3d bluff body*. Proceedings of AIMETA XXII, Genova 14-17 Sept 2015.

[9] G. I. Taylor, *Statistical theory of turbulence. part I-IV*. Proceedings of the Royal Society of London A: Mathematical, Physical and Engineering Sciences, volume 151, pages 421478. The Royal Society, 1935.

[10] G. I. Taylor, *Statistical Theory of Turbulence. V. Effect of Turbulence on Boundary Layer Theoretical Discussion of Relationship between Scale of Turbulence and Critical Resistance of Spheres*. Proceedings of the Royal Society of London. Series A, Mathematical and Physical Sciences, 156(888), 307-317, 1936.

[11] M. Orazi, D. Lasagna, G. Iuso, *Circular Cylinder drag reduction using piezoelectric actuators*. Advanced in Aircraft and Spacecraft Science (2014), pp.27-41

[12] I. Rodrguez a, O. Lehmkuhl a,b, J. Chiva a, R. Borrell b, A. Oliva *On the flow past a circular cylinder from critical to super-critical Reynolds numbers: Wake topology and vortex shedding*. International Journal of Heat and Fluid Flow, 55 (2015) 91103

[13] R. J. Moffat, *Contributions to the theory of single-sample uncertainty analysis*. ASME, Transactions, Journal of Fluids Engineering 104.2 : 250-258, 1982.

[14] R. J. Moffat, *Describing the uncertainties in experimental results*. Experimental thermal and fluid science, 1(1), 3-17, 1988.

[15] J. S. Bendat and A. G. Piersol, *Random data Analysis and Measurements Procedures*, Willey-Interscience, 1986.

[16] A. Evrard, O. Cadot, V. Herbert, D. Ricot, R. Vigneron and J. Dlery, *Fluid force and symmetry breaking modes of a 3d bluff body with a base cavity*. Journal of Fluids and Structures, 61:99114, 2016.

[17] R. Volpe, P. Devinant, and A. Kourta, *Experimental characterization of the unsteady natural wake of the full-scale square back ahmed body: flow bi-stability and spectral analysis*. Experiments in Fluids, 56(5):122, 2015.